



Optical imaging of the stochastic nucleation kinetics and intrinsic activation energy of single spin-crossover nanoparticles

Shasha Liu^{a,b} and Wei Wang^{a,1}

Edited by Catherine Murphy, University of Illinois at Urbana-Champaign, Urbana, IL; received July 30, 2024; accepted October 3, 2024

Cooperative spin crossover (SCO) compounds are one of the most promising molecular bistable solids due to their intriguing thermal hysteresis phenomena around room temperature. It is well known that hysteresis is an essential kinetic effect, however, accurate assessment of the spin transition kinetics of SCO nanomaterials remains scarce. Herein, we developed a thermal-optical methodology to image the thermally induced spin transition kinetics of single SCO nanoparticles in a quantitative, repeatable, and high-throughput manner. Single-particle measurement revealed an intrinsic nucleation-dominated spin transition mechanism, where a highly stochastic nucleation process was clearly observed during the repeatable measurements. By quantifying the dependence of nucleation time on temperature, the activation energy barriers for nucleation were further extracted at a single particle level. Based on this foundation, the high throughput of the optical imaging not only contributed to uncovering the significant nanoparticle-to-nanoparticle heterogeneity, with implications for a negative correlation between apparent activation energy barriers for nucleation and size of the SCO nanoparticles, but also facilitated identifying a minority with high activation energy at least twice the average value. The extraordinary performance was then attributed to the fewer defects within their structures, as confirmed by further results from the *in situ* creation of defects by thermal ablation, thereby setting the lower limit for the intrinsic activation energy of ideal SCO crystals and promising their potential for future applications in high-performance molecular devices.

nucleation kinetics | activation energy barrier | single particle measurement | optical imaging | bistable nanoparticles

Cooperative spin crossover (SCO) compounds are promising molecular solids with potential applications in high-density information storage, sensors, and molecular memory devices (1–6). This potential arises from their thermal hysteresis phenomena around room temperature, conferring a memory effect and intriguing molecular bistability (7–9). In detail, the electronic states of SCO molecules can switch reversibly between the diamagnetic low-spin (LS) state and the paramagnetic high-spin (HS) state upon a suitable external perturbation, such as temperature, magnetic field, and light. Particularly, SCO materials with strong cooperative effects can exist both in the LS state and HS state under the very same conditions depending on their immediate history, as a result of the strong elastic interactions between molecules and characterized by the spectacular hysteresis loop in their spin transition curves. It is important to clarify that hysteresis is an essential kinetic effect since it occurs under a thermodynamically unstable condition, where a high energy barrier separating the LS and HS states ensures that the lifetime of the metastable state is virtually infinite (9–13). Therefore, for a deep understanding of the spin transition mechanisms and to better tailor SCO materials into functional devices, it is indispensable to accurately characterize the spin transition kinetics and quantitatively assess the energy barrier of the highly cooperative SCO materials.

So far, quantitative measurements of the intrinsic spin transition kinetics and energy barriers remain scarce, mainly limited by two reasons. First, there are very few robust SCO crystals that can be utilized for repeatable measurements. Visible damage, such as cracks and fractures, are commonly investigated in highly cooperative SCO crystals during multiswitching cycles (14, 15). However, the spin transition in cooperative SCO materials is well acknowledged through a stochastic nucleation-to-growth mechanism, resulting in the kinetics obtained from one or several measurements potentially deviating from their intrinsic properties (16–19). In addition, multi-measurements are also required to determine the energy barrier for spin transition. Recent reports reveal that size reduction might provide a promising way to improve the robustness of SCO entities because small particles have a better resilience to effectively release the internal stress generated by the structural mismatch between the two states during the spin transition (9, 20).

Significance

Memory devices at the molecular level rely on bistable solids with large hysteresis in their transition behavior. However, the intrinsic first-order phase transition kinetics have been opaque. A thermal-optical method is developed that demonstrates the capability to accurately quantify the thermally induced nucleation-to-growth transition kinetics and the corresponding activation energy barriers of single spin-crossover nanoparticles. The results provide the experimental evidence of the stochastic nucleation behavior during repeatable spin transitions. Through high-throughput experiments, a subpopulation of nanoparticles with extraordinary performance is identified.

Author affiliations: ^aState Key Laboratory of Analytical Chemistry for Life Science, Chemistry and Biomedicine Innovation Center, School of Chemistry and Chemical Engineering, Nanjing University, Nanjing 210023, China; and ^bShenzhen Research Institute of Nanjing University, Shenzhen 518000, China

Author contributions: S.L. and W.W. designed research; S.L. performed research; S.L. analyzed data; S.L. wrote the paper; W.W. conceived the project; and W.W. supervised the research.

The authors declare no competing interest.

This article is a PNAS Direct Submission.

Copyright © 2024 the Author(s). Published by PNAS. This article is distributed under [Creative Commons Attribution-NonCommercial-NoDerivatives License 4.0 \(CC BY-NC-ND\)](#).

¹To whom correspondence may be addressed. Email: wei.wang@nju.edu.cn.

This article contains supporting information online at <https://www.pnas.org/lookup/suppl/doi:10.1073/pnas.2415379121/-DCSupplemental>.

Published November 13, 2024.

Second, there is a lack of suitable techniques to obtain intrinsic spin-transition kinetics, especially for SCO nanoparticles. Limited by the sensitivity of commonly used techniques, such as superconducting quantum interference devices and differential scanning calorimetry, bulk samples in the amount of at least several milligrams are usually required to generate a sufficiently large signal. As a consequence, the obtained results are indeed a combination of intrinsic spin transition kinetics of SCO materials and thermal transfer dynamics of the system, since it takes minutes for milligram-scale samples to reach thermal equilibrium. Moreover, the significant heterogeneity among individual particles is also masked by ensemble measurements because they only deliver an average response of bulk samples that include millions of nanoparticles, which is crucial for uncovering the structure-kinetics correlations as well as for screening out entities with extraordinary performance (21, 22). To comprehensively assess the intrinsic spin transition kinetics, it is highly desirable, but yet to be demonstrated, to characterize the transition kinetics of SCO nanoparticles with a reduced sample amount, ideally at the single particle level and in a repeatable manner.

The past decade has witnessed the great development of optical microscopy in observing the activity of single entities, including the spin transition of single particles, owing to their excellent sensitivity, sufficient spatiotemporal resolution, and diversified spectroscopic principles (23–27). The most commonly used strategy is tracking the change of physical properties of the single SCO crystals accompanied by the change of spin state, such as color, volume, and refractive index (9, 28–31). Bousseksou and coworkers first experimentally imaged and regulated the heterogeneous nucleation behavior of single SCO crystals by tracking the color change with the bright-field microscope (32, 33). With a similar methodology, Boukheddaden et al. studied the reversible spin transition dynamics of single SCO crystals (34, 35). Although promising, these observations mostly focus on the transition behaviors of big SCO particles with a size of hundreds of micrometers. We recently demonstrated the capability of surface plasmon resonance microscopy to measure the transition curves of single SCO nanoparticles by tracking their refractive index change upon temperature, where excellent spin transition stability after over 10,000 cycles was verified (22). Refractive index sensitive dark-field microscopy (DFM) was also introduced to study the thermal-induced phase transition kinetics of single inorganic and organic nanoparticles and exhibits unique advantages in high-throughput measurements for structure-kinetics correlation explorations (36–38).

In the present study, we employed a home-built temperature-controllable DFM to characterize the intrinsic spin transition kinetics of single SCO nanoparticles in a quantitative, reproducible, and high-throughput manner. Upon a temperature jump, it was found that the LS-HS transition of single SCO nanoparticles was triggered by a slow induction of nucleation (tens of seconds) followed by an extremely fast growth process (a few milliseconds). Taking advantage of single particle measurements and the robustness of the SCO nanoparticles, a highly stochastic nucleation time during the successive spin transitions was experimentally observed. By analyzing the dependence of nucleation time on temperature, another important thermodynamic parameter, the activation energy for nucleation (E_a) was also quantified at a single nanoparticle level. Based on this foundation and taking advantage of the high throughput of the DFM, the spin transition kinetics (nucleation time and E_a) of tens of individual SCO-NPs were screened in one experiment, where a significant nanoparticle-to-nanoparticle heterogeneity was clearly observed. This result not only contributed to revealing a negative dependence between E_a and size by

further correlating the structure features and spin transition kinetics of the same SCO nanoparticles via a bottom-up strategy but also facilitated the identification of entities with extraordinarily high E_a . Intriguingly, the high E_a of the identified SCO-NPs finally converged to the average value after in situ creating artificial defects by thermal ablation, and the dependence between E_a and size accordingly disappeared. These results not only confirmed that the nucleation of SCO nanoparticles was greatly regulated by defects within their structures but also highlighted the importance of the developed method in identifying individual particles with no or very few defects, thereby revealing the intrinsic E_a of highly cooperative SCO materials.

Results

[Fe(Htrz)₂(trz)](BF₄) was selected as a model material because it is one of the most studied SCO compounds due to the wide hysteresis loop around room temperature and well-established techniques for synthesizing it into nanoparticles (39–42). [Fe(Htrz)₂(trz)](BF₄) nanoparticles, referred as to SCO-NPs hereafter, were prepared by the conventional reverse micelle method according to the previous report (39). The as-synthesized SCO-NPs exhibited a light purple color at room temperature (293 K), corresponding to an absorption band centered at 540 nm in its absorption spectrum resulting from the ¹A₁–¹T₁ transition of Fe(II) (*SI Appendix, Fig. S1*). Upon heating to approximately 380 K, the color of the SCO-NPs transitioned into white, a typical indicator of the LS–HS transition (39). The thermal transition curves of single SCO-NPs were further characterized using our previously developed methodology, where a wide hysteresis loop over 50 K at around 350 K was clearly observed (*SI Appendix, Fig. S2*). Scanning electron microscopy (SEM) reveals the cubic nanoparticles with a broad size distribution spanning from 100 nm to 500 nm (*SI Appendix, Fig. S3*). These results are consistent with previous reports, suggesting the successful synthesis of the SCO-NPs (22, 39, 43).

In order to optically image the thermal-induced transition kinetics of single SCO-NPs, the apparatus was built by integrating a microarea heating system into the DFM (Fig. 1*A*). Specifically, for the microheating system, the key component is a home-fabricated chip, which functions to support and regulate the temperature of the SCO-NPs. The chip was made by sputtering a thin layer of gold film with a specific pattern onto the coverslip, where the gold film acted as a resistor to heat the SCO-NPs via the Joule effect and the pattern was designed to limit the effective heating area within 500 × 500 μm². The chip has been shown to exhibit excellent compatibility with the optical imaging setup and to effectively balance the influence of temperature changes on the stability of the imaging system and the throughput of the technique. More details can be found in our previous reports (36, 37). The other big part of the apparatus is the DFM for monitoring the thermal-induced spin transition of single SCO-NPs, taking advantage of the refractive index change of the SCO-NPs accompanied by the spin switching (44). The DFM was built based on a commercial Ti-2E inverted microscope and a light-emitting diode (LED) with a central wavelength of 540 nm was employed to light up the SCO-NPs. The light scattered by SCO-NPs was finally collected by a camera after passing through the objective, resulting in a typical DFM image where each bright spot represents an individual SCO-NP (Fig. 1*A*). The reason for selecting the 540 nm-LED is to enhance the disparity in optical intensity between two spin states, thereby augmenting the sensitivity of the developed methodology.

In a typical experiment, the SCO-NPs were first sealed in a chamber filled with dry nitrogen to avoid the possible influence of

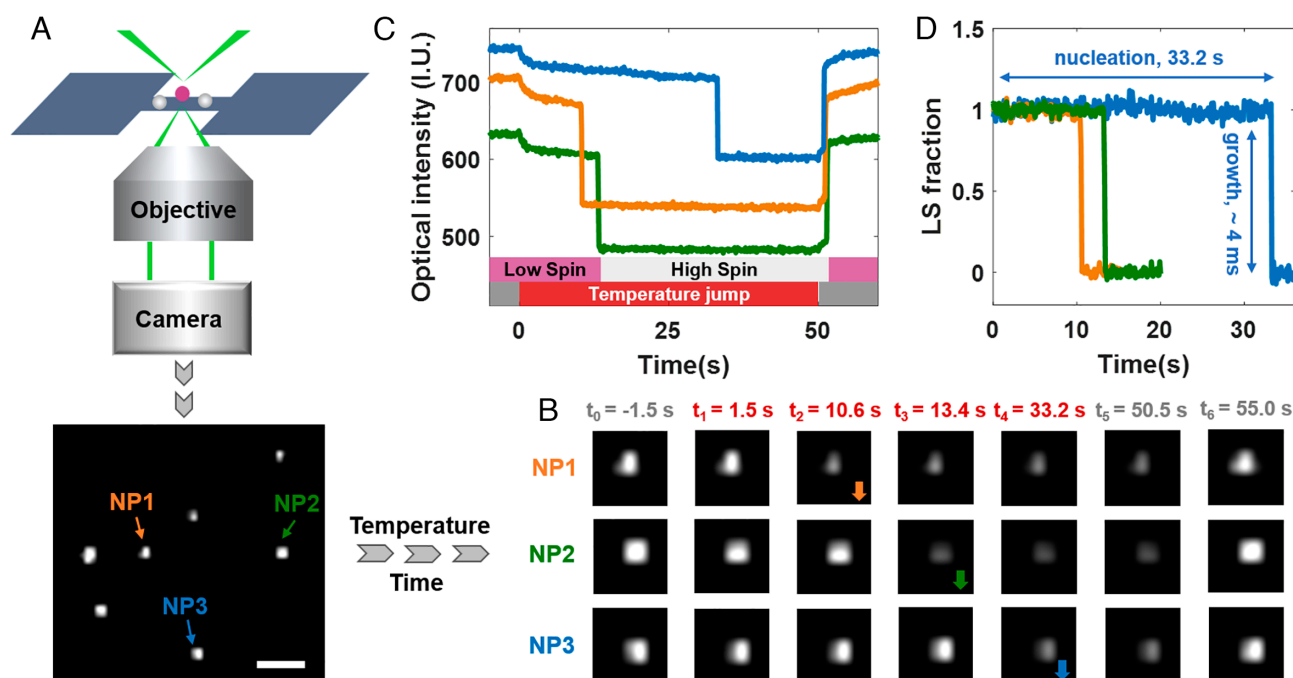


Fig. 1. Optical imaging of the isothermal spin transition kinetics of single SCO-NPs. (A) Schematic diagram of the experimental setup. (Scale bar, 3 μm .) (B) Representative snapshots of three SCO-NPs during a typical temperature jump process. The temperature jump from 293.0 to 370.8 K was applied to SCO-NPs at $t = 0.0$ s and was released at $t = 50.0$ s. (C and D) Corresponding optical curves and spin transition curves of the three SCO-NPs shown in B.

humidity on the spin transition. At room temperature (293.0 K), the optical scattering intensity of all SCO-NPs was kept constant (Fig. 1B and C, $t_0 = -1.5$ s), indicating the SCO-NPs remain stable LS state. At a certain moment ($t = 0.0$ s), a temperature jump from 293.0 K to 370.8 K was applied to the SCO NPs. Immediately, a gradual decrease in the optical intensity was synchronously observed in all particles ($t_1 = 1.5$ s), evidencing that the temperature of SCO-NPs was successfully modulated and will be discussed later. The camera continuously recorded the DFM images during the entire process at a rate of 10 frames per second (fps). The snapshots of three representative SCO-NPs are shown in Fig. 1B. After the incubation at 370.8 K for 10.6 s (t_2), a steep drop in the optical intensity of NP1 was clearly observed, representing the growth of the new phase, i.e., HS state. This point was supported by the results as follows. i) NP2 and NP3 also showed a similar steep drop in their optical intensity curves but with different induction times of 13.4 s (t_3) and 33.2 s (t_4), respectively. Plus, the optical intensity of all three SCO-NPs returned to their original intensity after releasing the temperature jump ($t_6 = 55.0$ s). We note that the short induction time (~ 1 s) for the HS-LS transition is because the temperature jump (293.0 K) used herein is much lower than its HS-LS transition temperature (~ 315 K, *SI Appendix, Fig. S2*). ii) The decreased optical intensity ($\sim 15\%$) is well consistent with the calculated decreased scattering cross-section ($\sim 13\%$) according to the Mie scattering theory (45). iii) In the control experiment of the SiO_2 nanosphere, no steep drop but the very same gradual decrease signal is observed in its optical intensity curves as shown in *SI Appendix, Fig. S4*. This observation also evidenced the gradual decrease in the optical intensity after the application of the temperature jump was a side effect of the temperature change of the system, which was attributed to the physical focal drift of the DFM caused by the refractive index change of the substrate during the heating process. It was further supported by the consistency between the change in the decreased optical intensity and temperature change of the substrate during cyclic heating-cooling processes (*SI Appendix, Fig. S5*).

Therefore, the signal can serve as an indicator of changes in system temperature and also a reference to obtain the net response of the spin transition in SCO-NPs after subtraction (Fig. 1D and *SI Appendix, Fig. S4*).

Fig. 1D suggests that the isothermal spin transition kinetics of all three SCO-NPs follow a nucleation and growth process, confirming the spin transition as a first-order phase transition at a single nanoparticle level (9). Specifically, as the temperature of the SCO-NPs increased, they began to form domains with the HS state in a microscopic and probabilistic manner, a process denoted as nucleation. Due to the limited number of molecules transitioning to the HS state, the change in the refractive index of the entire particle was extremely small and back-and-forth, resulting in an undetectable change in the optical intensity of the SCO-NPs. Driven by interactions among the switched molecules, the domains eventually stabilized at random moments and subsequently grew to a macroscopic phase (growth), leading to a dramatic decrease in the optical intensity of SCO-NPs. Moreover, the nucleation time (time length between applying the temperature jump and the formation of the new phase, 33.2 s for NP3) was much longer than the growth time (time length between the beginning and end of the formation of the new phase, <0.1 s for NP3), suggesting the LS-HS transition of SCO-NPs was a nucleation-determined process. Since the growth of the HS phase was too fast beyond the temporal resolution used in this measurement, we further employed a fast camera with a temporal resolution of 2 ms to quantify the propagation kinetics of the HS phase in SCO-NPs (*SI Appendix, Fig. S6*). The result indicated that it took only 4 ms for the SCO-NPs with a size of about 400 nm to complete the growth of the new phase at 370.8 K. The velocity for LS/HS transformation was accordingly calculated to be 100 $\mu\text{m/s}$, which is comparable to the results obtained from the single-particle measurement of microcrystals but much larger than those obtained by ensemble measurements (9, 46). In order to clarify this, we simply simulated the ensemble measurement by averaging the optical curves of tens of SCO-NPs including the three SCO-NPs shown in Fig. 1B. *SI Appendix, Fig. S7* shows the calculated average LS-HS transition

kinetics still follow the nucleation-and-growth process, but the growth dynamic is greatly widened (from 4 ms to 8.0 s). The velocity was accordingly determined to be 0.04 $\mu\text{m/s}$ by dividing the average size of SCO-NPs (300 nm) by the determined growth time (8.0 s), which severely deviates from the intrinsic spin transition kinetics of SCO-NPs. These results evidence the importance of the single-particle measurement in revealing the intrinsic spin transition kinetics of SCO materials.

Based on the intrinsic spin transition kinetic of SCO-NPs obtained from every single measurement and taking advantage of the robustness of SCO-NPs, a highly stochastic nature of the nucleation in the spin transition was experimentally investigated during repeatable measurements. The same temperature jump was successively applied to SCO-NPs, consisting of a 50 s heating step (to induce the LS–HS transition) followed by a 50 s cooling step (to drive the SCO-NPs return to the original LS state). When plotting the LS–HS transition curves of 20 cycles, significant heterogeneity in the nucleation time among cycles is clearly observed in Fig. 2A (blue curves) and *SI Appendix, Fig. S8*. The corresponding histogram of the nucleation time features a typical Gaussian distribution (Fig. 2B, blue bars), suggesting the independent random nucleation behavior of SCO-NPs in spin transitions during the repeatable measurements. In contrast, the optical intensity of the SCO-NPs remained identical for each cycle through the whole measurements, verifying the robustness of the SCO-NPs and thus the reliability of the observed stochastic nucleation behavior. Temperature fluctuations were further excluded as a possible influence on the

observed randomness of nucleation time based on the following results. First, the recorded temperature jumps among cycles were well consistent with each other (*SI Appendix, Fig. S9*). It is reasonable because the temperature of the SCO-NPs herein is controlled by the voltage applied to the substrate and the electrochemical workstation offers a voltage control with accuracies within 0.1%, which is much smaller than that of the nucleation time (>10%). Second, the randomness of the nucleation time decreases as temperature increases as shown in Fig. 2B and *SI Appendix, Fig. S10*, which is contrary to the fact that temperature fluctuation increases with a higher absolute temperature. Additionally, it is worth noting that the transition curves used herein for stochastic analysis involve 11 to 30 cycles during successive measurements to mitigate the impact of uncommon spin transition behavior in the first or first several cycles (*SI Appendix, Fig. S8*) (8).

Another characteristic of spin transition is highly temperature dependent. It is clear that the nucleation time for LS–HS transition decreases as the heating temperature increases as shown in Fig. 2C. This is sensible because the driving force for spin transition originates from the free energy difference between the two states and the LS–HS transition is indeed an entropy-driven process (9). The nucleation time was then quantitatively extracted by fitting the distribution of nucleation time with the Gaussian function. When plotting the nucleation time with the corresponding temperature, it was found that the increase in temperature reduced the nucleation time in an exponential dependence. A linear dependence of the logarithm of nucleation rate (reciprocal of nucleation time) on the

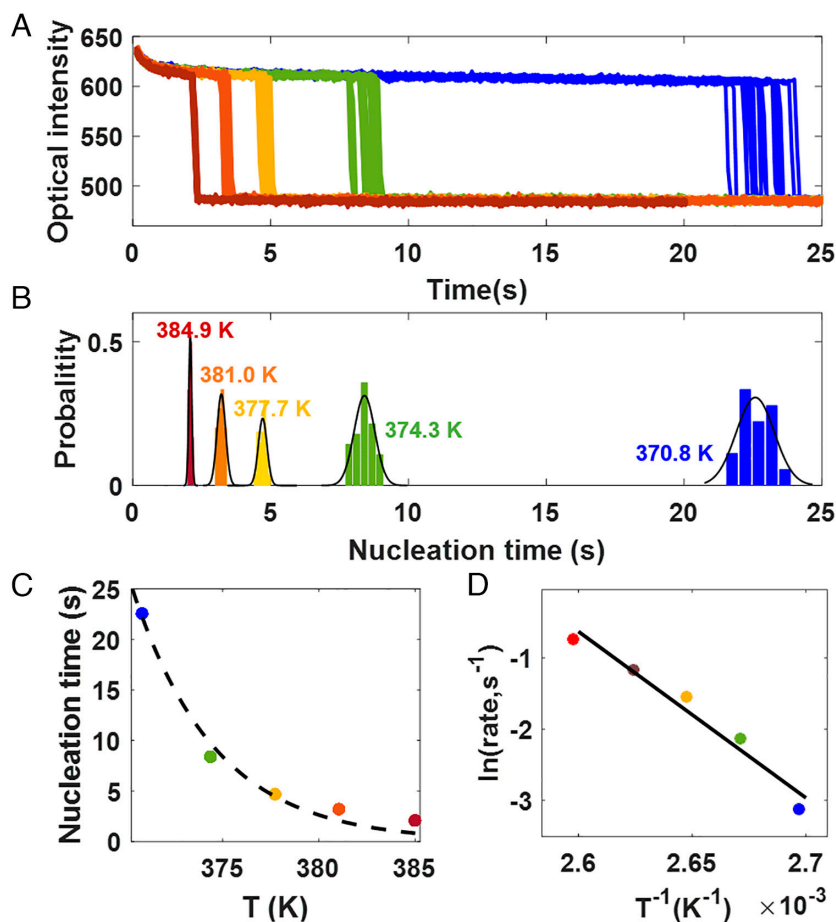


Fig. 2. Determination of the activation energy barrier for nucleation of a single SCO-NP. (A) Optical curves of the very same SCO-NP under different temperature jumps. The red lines, orange lines, yellow lines, green lines, and blue lines represent the results obtained at temperature jumps from 293.0 to 384.9 K, 381.0 K, 377.7 K, 374.3 K, and 370.8 K, respectively. For each temperature jump, results from 20 repeatable measurements. (B) The corresponding histogram of the nucleation time at different temperature jumps. (C) The scatter plot of the average nucleation time as a function of temperature jump. (D) The logarithm of the nucleation rate vs. T^{-1} and their linear dependence allows for determining the E_a for nucleation of single SCO-NPs according to the Arrhenius equation.

reciprocal of temperature is also observed in Fig. 2D, where the slope is further used to determine the activation energy for nucleation (E_a , 194 kJ/mol) according to the Arrhenius equation. The linear dependence was also observed in other SCO nanoparticles, $[\text{Fe}(\text{Atrz})_3]\text{Br}_2$, further validating the reliability and general applicability of the developed methodology (*SI Appendix*, Fig. S11).

While it is generally accepted that the spin transition kinetics is particle-dependent due to the structural heterogeneity among individual particles, the correlation between the E_a and structure is largely unexplored (22, 29). By taking advantage of the high throughput of the DFM, a correlation between the E_a for nucleation in the LS–HS transition and the size of the SCO-NPs was built via a bottom–up strategy. Fig. 3A demonstrates one typical DFM image with a field of view of $\sim 100 \times 100 \mu\text{m}^2$ including tens of SCO-NPs, meaning that the spin transition kinetics of all SCO-NPs in the field of view can be obtained from one experiment. The SCO-NPs were evenly dispersed on the substrate with a distance of more than a few micrometers between each other to ensure that the optical responses from different particles can be distinguished in the DFM images, as the spatial resolution of the current DFM setup is determined to be approximately 600 nm according to diffraction theory. The corresponding SEM image shown in Fig. 3A suggests that the SCO-NPs with a bigger size have a higher optical intensity at room temperature. Therefore, the size of each SCO-NP can also be estimated from its original optical intensity according to a previously established calibration curve (*SI Appendix*, Fig. S12). Note that the minimum size of SCO-NPs that could be reliably studied by the current setup was assessed to be about 100 nm, which could be potentially improved to study the SCO-NPs as small as 10 nm in future studies with optimized DFM set-up (*SI Appendix*, Fig. S13). When plotting the E_a and the corresponding size of each SCO-NP in the view, a statistically negative correlation was uncovered from the significantly heterogeneous SCO-NPs (Fig. 3B and C). It may be attributed to the fact that larger SCO-NPs are more likely to have more defects introduced during the sample synthesis and preparation, which can function as nucleation sites with a lower E_a . On the other hand,

some exceptional SCO-NPs whose E_a are greatly larger than the average value of all SCO-NPs (indicated as the black rectangle in Fig. 3B) were also discovered from the single particle level. For example, the E_a of the SCO-NP marked by the blue circle is approximately twice that of the one marked by the black circle (whose E_a is very close to the average value), despite their similar sizes. The uncovered minorities with high E_a not only promise a bright future for the applications of cooperative SCO materials due to their prolonged lifetime of the metastable state but also serve as ideal samples for further elucidation of the underlying mechanisms.

To get a deeper understanding of why a minority of SCO-NPs exhibit excellent performance as well as of how size influences the nucleation of SCO-NPs, the E_a of the very same SCO-NPs were quantified and compared before and after the in situ regulation, taking advantage of the excellent spatial resolution as well as in situ optical measurement, a capability that has never been demonstrated before. After the first E_a measurement, all SCO-NPs were further incubated under a high-temperature (473 K) N_2 chamber for 200 s to create defects within their structures via thermal ablation artificially (32). One of the most noticeable changes in the SCO-NPs after thermal ablation is an irreversible decrease in their optical scattering intensity (Fig. S14), indicating the successful removal of the matter from the SCO-NPs and thus the injection of the new defects. As a consequence, the temperature of the LS–HS transition decreased by approximately 20 K (*SI Appendix*, Fig. S15), which is consistent with the pioneering report (32). Subsequently, we redetermined and compared the E_a of the same SCO-NPs before and after the in situ regulation, it was found that the E_a of the majority decreased after the thermal ablation (Fig. 4A and *SI Appendix*, Fig. S16). Intriguingly, the previously observed negative dependence between E_a and the size disappeared after the creation of “artificial defects” in all SCO-NPs (Fig. 4B), verifying the speculation that the negative dependence originates from the heterogeneous “native defects” among individual particles with different sizes. More importantly, after the thermal ablation, the E_a variation among the SCO-NPs with a similar size was also significantly narrowed. The E_a

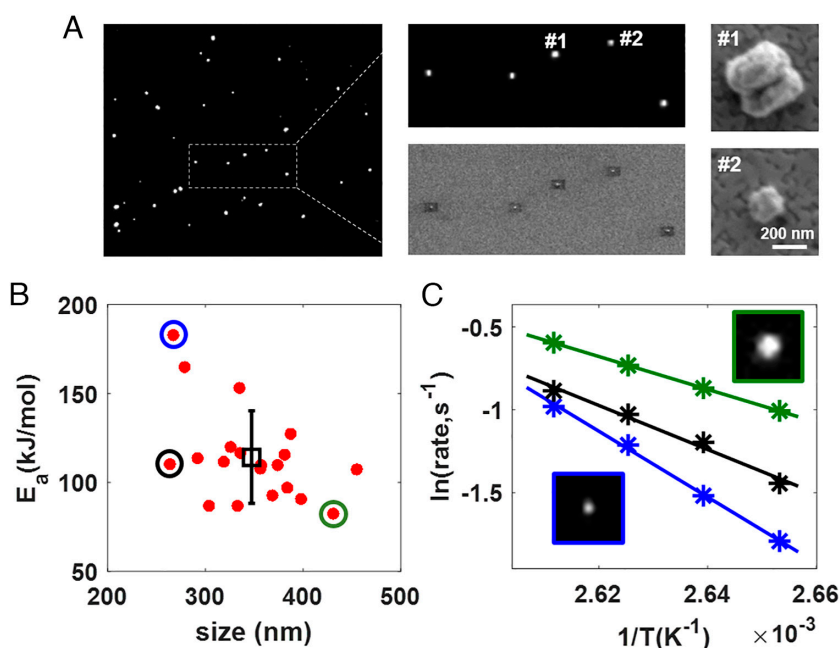


Fig. 3. Exploration of the correlations between size and activation energy for nucleation of SCO-NPs via a bottom–up strategy. (A) Corresponding DFM and the SEM image of the same SCO-NPs. (B) Scatter plot of E_a for nucleation in SCO-NPs as a function of their corresponding size. The black rectangle indicates the average E_a of all SCO-NPs shown in B. (C) The logarithm of the nucleation rate vs. T^{-1} of three representative SCO-NPs marked by a black circle (has an E_a close to the average value), blue circle (has an E_a greatly larger than the average value but with a similar size as the one marked by the black circle), and green circle (has an E_a smaller than average value) in B. The *Inset* images show the corresponding DFM images of the SCO-NPs.

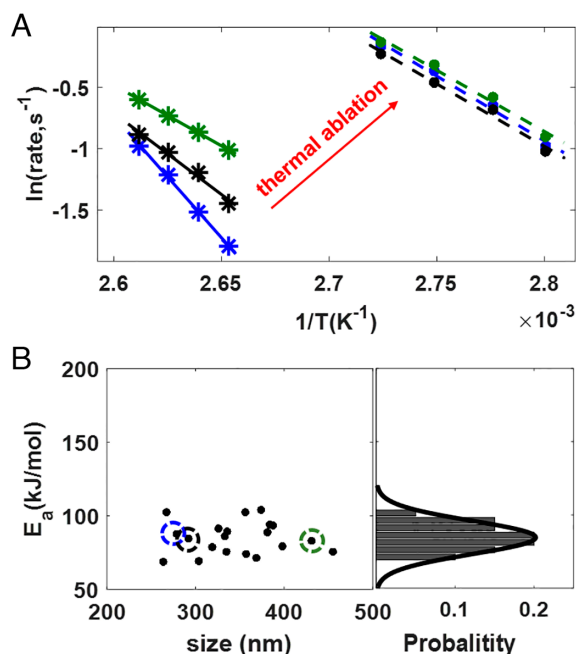


Fig. 4. Comparison of the spin transition kinetics of the very same SCO-NPs before and after in situ thermal ablation. (A) The logarithm of the nucleation rate vs. T^{-1} for the three SCO-NPs before (solid lines) and after (dash lines) in situ creating of artificial defects by thermal ablation at 473 K for 200 s. (B) The corresponding scatter plot of E_a and the size of the same SCO-NPs shown in Fig. 3B after the thermal ablation. The histogram on the Right panel shows the corresponding statistical result of the E_a .

of all SCO-NPs converged to an average value of ~ 90 kJ/mol regardless of their size and morphology, representing an apparent activation energy for the nucleation in the LS–HS transition of the commonly used defect-ridden SCO materials. The identified SCO-NPs with an E_a at least twice higher than the average value were thus attributed to the fewer defects within their structures, thereby setting the lowest limit of the intrinsic E_a for nucleation of the ideal SCO crystals. These results not only reveal that the nucleation process of SCO-NPs is essentially determined by the intrinsic properties of the material and greatly influenced by the defects within the particles, but also highlight the crucial importance of high-throughput screening of the intrinsic spin transition kinetics of SCO-NPs from a single particle level, for a better understanding of the transition mechanisms and the validation of their potential for future applications.

Discussion

We developed a unique thermal-optical methodology to characterize and in situ regulate the thermal-induced spin transition kinetics of single SCO nanoparticles in a quantitative, repeatable, and high-throughput manner. Single-particle measurement first allowed us to obtain an intrinsic thermal-induced nucleation-dominated spin transition kinetics and the activation energy barrier for nucleation of single SCO-NPs, by excluding the averaging effect of ensemble measurements on the transition kinetics and the thermal equilibrium of bulk samples containing millions of SCO entities. Based on this foundation, the stochastic nucleation behavior in the spin

transition of single SCO-NPs was experimentally observed. Taking advantage of the excellent spatial resolution and high-throughput of the optical measurement, the size-nucleation activation energy correlations were further uncovered and in situ regulated via a bottom–up strategy, revealing that the nucleation behavior of the SCO-NPs was essentially governed by the intrinsic properties of the material and greatly influenced by the defects within SCO entities. The identified minority with extraordinary activation energy barriers reveals the intrinsic high activation energy for nucleation of the ideal SCO crystals and thus promises their potential for future applications. Given that the developed technique tracks changes in the refractive index of the particle—an inherent property of materials—and considering the potential improvements in size detection limit and spatiotemporal resolution, we foresee the applications of the present methodology in revealing the intrinsic thermal transition kinetics in many promising thermal-induced phase transitions.

Materials and Methods

Materials and Characterizations. $[\text{Fe}(\text{Htrz})_2(\text{trz})](\text{BF}_4)$ nanoparticles were prepared by the conventional reverse micelle method according to previous reports (39). Then, 5 mg ascorbic acid (Sigma) was first dissolved in the 0.8 mL deionized water (18.2 MΩ cm), and 337 mg $\text{Fe}(\text{BF}_4)_2$ (Alfa Aesar) was then added to serve as solution 1. Solution 2 was made by adding 207 mg 1,2,4-trizole (Heowns) into 0.8 mL deionized water. After adding 0.8 mL surfactant (Tergitol-NP9, Sigma), the two solutions were quickly mixed and maintained in an ultrasonic agitation for 10 min at 50 °C to induce the growth of the particles. The powder was finally obtained after washing the precipitates with ether twice and drying them in the vacuum oven overnight. SEM (Phenom) and UV-vis spectroscopy (Shimadzu UV-3600) were used to characterize the as-synthesized SCO-NPs. The substrate used herein for supporting and heating SCO-NPs was fabricated by Electromagnetic sputtering (HIPIMS, GCEMarket). The detailed geometry of the gold layer was described in our previous work and was achieved by photolithography (SU-8).

Sample Preparation. A trace amount of SCO-NP powder was dispersed in 1 mL ethanol (AR, SCR), and then, 20 μL of SCO-NP suspension was dropped onto the home-fabricated substrate. The sample was dried in a glovebox filled with N_2 (Mikrouna) for 24 h and encapsulated before the optical measurements.

Temperature-Controllable DFM. DFM was built on an inverted optical microscopy (Nikon, Ti-2E), equipped with a 20 \times objective (N.A. = 0.45) and a dry DFM condenser (N.A. = 0.95 to 0.80). Scattered light from the SCO-NPs was collected by a CCD camera (Pike F-032B, Allied Vision Technologies) or a fast camera (MEMRECAM GX-8F) with an acquisition rate of 10 and 500 fps, respectively. An electrochemical workstation (CS120, Corrtest) was used to apply voltage on the substrate, and the value of applied voltage was controlled by a wave function generation (Rigol). A data acquisition card USB-6251 (DAQ, National Instruments) was used to synchronize the voltage applied on the gold film and the optical DFM intensity of SCO-NPs acquired by the CCD.

Data, Materials, and Software Availability. All study data are included in the article and/or supporting information.

ACKNOWLEDGMENTS. We acknowledge the financial support from the National Natural Science Foundation of China (Nos. 21925403, 22327803, 22304078), Natural Science Foundation of Jiangsu Province (BK20230774), the Excellent Research Program of Nanjing University (Grant ZYJH004), Jiangsu Funding Program for Excellent Postdoctoral Talent (2024ZB205) and Guangdong Basic and Applied Basic Research Foundation (2024A1515011331).

- O. Kahn, C. J. Martinez, Spin-transition polymers: From molecular materials toward memory devices. *Science* **279**, 44–48 (1998).
- K. Ridier *et al.*, Unprecedented switching endurance affords for high-resolution surface temperature mapping using a spin-crossover film. *Nat. Commun.* **11**, 3611 (2020).
- R. Torres-Cavanillas *et al.*, Spin-crossover nanoparticles anchored on MoS_2 layers for heterostructures with tunable strain driven by thermal or light-induced spin switching. *Nat. Chem.* **13**, 1101–1109 (2021).

- R. Torres-Cavanillas, M. Gavara-Edo, E. Coronado, Bistable spin-crossover nanoparticles for molecular electronics. *Adv. Mater.* **36**, 2307718 (2024).
- Y. Lu *et al.*, Tunable charge transport and spin dynamics in two-dimensional conjugated metal-organic frameworks. *J. Am. Chem. Soc.* **146**, 2574–2582 (2024).
- S. Mi, G. Molnár, K. Ridier, W. Nicolazzi, A. Bousseksou, All-atom molecular dynamics simulation of the $[\text{Fe}(\text{pyrazine})]\text{Ni}(\text{CN})_4$ spin-crossover complex. II. Spatiotemporal study of a bimorph actuator. *Phys. Rev. B* **109**, 054104 (2024).

7. A. Bousseksou, G. Molnár, L. Salmon, W. Nicolazzi, Molecular spin crossover phenomenon: Recent achievements and prospects. *Chem. Soc. Rev.* **40**, 3313–3335 (2011).
8. S. Brooker, Spin crossover with thermal hysteresis: Practicalities and lessons learnt. *Chem. Soc. Rev.* **44**, 2880–2892 (2015).
9. K. Ridier, G. Molnár, L. Salmon, W. Nicolazzi, A. Bousseksou, Hysteresis, nucleation and growth phenomena in spin-crossover solids. *Solid State Sci.* **74**, A1–A22 (2017).
10. A. Pal, M. Sitti, Programmable mechanical devices through magnetically tunable bistable elements. *Proc. Natl. Acad. Sci. U.S.A.* **120**, e2212489120 (2023).
11. M. B. Bushuev, E. B. Nikolaenkova, V. P. Krivopalov, Non-isothermal kinetics of spin crossover. *Phys. Chem. Chem. Phys.* **19**, 16955–16959 (2017).
12. M. B. Bushuev, Kinetics of spin crossover with thermal hysteresis. *Phys. Chem. Chem. Phys.* **20**, 5586–5590 (2018).
13. K. Ridier *et al.*, Temporal separation between lattice dynamics and electronic spin-state switching in spin-crossover thin films evidenced by time-resolved X-ray diffraction. *Adv. Funct. Mater.* **34**, 2403585 (2024).
14. A. Slimani *et al.*, Visualization and quantitative analysis of spatiotemporal behavior in a first-order thermal spin transition: A stress-driven multiscale process. *Phys. Rev. B* **84**, 094442 (2011).
15. P. Chakraborty *et al.*, Optical microscopy imaging of the thermally-induced spin transition and isothermal multi-stepped relaxation in a low-spin stabilized spin-crossover material. *Phys. Chem. Chem. Phys.* **24**, 982–994 (2022).
16. N. Huby *et al.*, Photoinduced spin transition probed by x-ray diffraction. *Phys. Rev. B* **69**, 020101 (2004).
17. A. Slimani, K. Boukheddaden, K. Yamashita, Effect of intermolecular interactions on the nucleation, growth, and propagation of like-spin domains in spin-crossover materials. *Phys. Rev. B* **92**, 014111 (2015).
18. K. Ridier *et al.*, Spatiotemporal dynamics of the spin transition in [Fe(HB(trz)₃)] single crystals. *Phys. Rev. B* **96**, 134106 (2017).
19. I. Gudyma, A. Maksymov, M. Dimian, Stochastic kinetics of photoinduced phase transitions in spin-crossover solids. *Phys. Rev. E* **88**, 042111 (2013).
20. S. Mi, K. Ridier, G. Molnár, W. Nicolazzi, A. Bousseksou, Effects of the surface energy and surface stress on the phase stability of spin crossover nano-objects: A thermodynamic approach. *Nanoscale* **16**, 7237–7247 (2024).
21. S. Bedoui *et al.*, Impact of single crystal properties on nucleation and growth mechanisms of a spin transition. *Polyhedron* **87**, 411–416 (2015).
22. S. Liu *et al.*, Imaging the thermal hysteresis of single spin-crossover nanoparticles. *J. Am. Chem. Soc.* **142**, 15852–15859 (2020).
23. M. Zhao *et al.*, Long-range enhancements of micropollutant adsorption on metal-promoted photocatalysts. *Nat. Catal.* **7**, 912–920 (2024), 10.1038/s41929-024-01199-0.
24. C. Liu *et al.*, Single polymer growth dynamics. *Science* **358**, 352–355 (2017).
25. J. Chen *et al.*, Measuring the activation energy barrier for the nucleation of single nanosized vapor bubbles. *Proc. Natl. Acad. Sci. U.S.A.* **116**, 12678–12683 (2019).
26. R. Traiche *et al.*, Spatiotemporal observation and modeling of remarkable temperature scan rate effects on the thermal hysteresis in a spin-crossover single crystal. *J. Phys. Chem. C* **121**, 11700–11708 (2017).
27. M. Sy *et al.*, Structure-driven orientation of the high-spin-low-spin interface in a spin-crossover single crystal. *Angew. Chem. Int. Ed. Engl.* **53**, 7539–7542 (2014).
28. J. J. Zakrewski, M. Liberka, J. Wang, S. Chorazy, S.-I. Ohkoshi, Optical phenomena in molecule-based magnetic materials. *Chem. Rev.* **124**, 5930–6050 (2024).
29. R. M. van der Veen, O.-H. Kwon, A. Tissot, A. Hauser, A. H. Zewail, Single-nanoparticle phase transitions visualized by four-dimensional electron microscopy. *Nat. Chem.* **5**, 395–402 (2013).
30. G. Molnár, A. Bousseksou, A. Zwick, J. J. McGarvey, The spin-crossover phenomenon in the solid state: Do domains play a role? A micro-Raman study. *Chem. Phys. Lett.* **367**, 593–598 (2003).
31. B. T. Flinn *et al.*, Sensing the spin state of room-temperature switchable cyanometallate frameworks with nitrogen-vacancy centers in nanodiamonds. *ACS Nano* **18**, 7148–7160 (2024).
32. S. Bedoui *et al.*, Laser-induced artificial defects (LIADs): Towards the control of the spatiotemporal dynamics in spin transition materials. *Adv. Mater.* **24**, 2475–2478 (2012).
33. V. M. Hiiuk *et al.*, Influence of the ultra-slow nucleation and growth dynamics on the room-temperature hysteresis of spin-crossover single crystals. *Chem. Phys. Lett.* **770**, 138442 (2021).
34. M. Paez-Espejo, M. Sy, K. Boukheddaden, Unprecedented bistability in spin-crossover solids based on the retroaction of the high spin low-spin interface with the crystal bending. *J. Am. Chem. Soc.* **140**, 11954–11964 (2018).
35. M. Sy *et al.*, Reversible control by light of the high-spin low-spin elastic interface inside the bistable region of a robust spin-transition single crystal. *Angew. Chem. Int. Ed. Engl.* **55**, 1755–1759 (2016).
36. S. Liu *et al.*, Spontaneous takeoff of single sulfur nanoparticles during sublimation studied by dark-field microscopy. *J. Am. Chem. Soc.* **145**, 3987–3993 (2023).
37. S. Liu *et al.*, Optical imaging of the molecular mobility of single polystyrene nanospheres. *J. Am. Chem. Soc.* **144**, 1267–1273 (2022).
38. W. Wang, Imaging the chemical activity of single nanoparticles with optical microscopy. *Chem. Soc. Rev.* **47**, 2485–2508 (2018).
39. E. Coronado, J. R. Galán-Mascarós, M. Monrabal-Capilla, J. García-Martínez, P. Pardo-Ibáñez, Bistable spin-crossover nanoparticles showing magnetic thermal hysteresis near room temperature. *Adv. Mater.* **19**, 1359–1361 (2007).
40. G. Gallé *et al.*, Study of the fast photoswitching of spin crossover nanoparticles outside and inside their thermal hysteresis loop. *Appl. Phys. Lett.* **102**, 063302 (2013).
41. F. Guillaume *et al.*, Photoswitching of the spin crossover polymeric material [Fe(Htrz)₂(trz)](BF₄) under continuous laser irradiation in a Raman scattering experiment. *Chem. Phys. Lett.* **604**, 105–109 (2014).
42. A. Diaconu *et al.*, Piezoresistive effect in the [Fe(Htrz)₂(trz)](BF₄) spin crossover complex. *J. Phys. Chem. Lett.* **8**, 3147–3151 (2017).
43. C. Etrillard, V. Faramarzi, J.-F. Dayen, J.-F. Letard, B. Doudin, Photoconduction in [Fe(Htrz)₂(trz)](BF₄)-H₂O nanocrystals. *Chem. Commun.* **47**, 9663–9665 (2011).
44. Y. Zhang *et al.*, A molecular spin-crossover film allows for wavelength tuning of the resonance of a Fabry-Perot cavity. *J. Mater. Chem. C* **8**, 8007–8011 (2020).
45. S. Zhu *et al.*, Light-scattering detection below the level of single fluorescent molecules for high-resolution characterization of functional nanoparticles. *ACS Nano* **8**, 10998–11006 (2014).
46. M. B. Bushuev *et al.*, A mononuclear iron(II) complex: Cooperativity, kinetics and activation energy of the solvent-dependent spin transition. *Dalton Transact.* **45**, 107–120 (2016).